

This is the accepted manuscript made available via CHORUS. The article has been published as:

Direct measurement of the static and transient magneto-optical permittivity of cobalt across the entire M-edge in reflection geometry by use of polarization scanning

Dmitriy Zusin, Phoebe M. Tengdin, Maithreyi Gopalakrishnan, Christian Gentry, Adam Blonsky, Michael Gerrity, Dominik Legut, Justin M. Shaw, Hans T. Nembach, T. J. Silva, Peter M. Oppeneer, Henry C. Kapteyn, and Margaret M. Murnane

Phys. Rev. B **97**, 024433 — Published 30 January 2018

DOI: [10.1103/PhysRevB.97.024433](https://doi.org/10.1103/PhysRevB.97.024433)

1 **Direct measurement of the static and transient magneto-optical**
2 **permittivity of cobalt across the entire M -edge in a reflection**
3 **geometry by use of polarization scanning**

4 Dmitriy Zusin,^{1,*} Phoebe M. Tengdin,¹ Maithreyi Gopalakrishnan,¹ Christian Gentry,¹
5 Adam Blonsky,¹ Michael Gerrity,¹ Dominik Legut,² Justin Shaw,³ Hans Nembach,³
6 T.J. Silva,³ Peter M. Oppeneer,⁴ Henry C. Kapteyn,¹ and Margaret M. Murnane¹

7 ¹*Department of Physics and JILA, University of Colorado, Boulder, CO 80309, USA*

8 ²*Nanotechnology & IT4Innovations Center,*

9 *VSB Technical University Ostrava, 708 33 Ostrava-Poruba, Czech Republic*

10 ³*Quantum Electromagnetics Division,*

11 *National Institute of Standards and Technology, Boulder, CO 80305, USA^b*

12 ⁴*Department of Physics and Astronomy,*

13 *Uppsala University, S-75120 Uppsala, Sweden*

^b Contribution of the National Institute of Standards and Technology; not subject to copyright in the United States. Certain commercial equipment, instruments, or materials are identified in this paper in order to specify the experimental procedure adequately. Such identification is not intended to imply recommendation or endorsement by NIST, nor is it intended to imply that the materials or equipment identified are necessarily the best available for the purpose.

Abstract

The microscopic state of a magnetic material is characterized by its resonant magneto-optical response through the off-diagonal dielectric tensor component ϵ_{xy} . However, the measurement of the full complex ϵ_{xy} in the extreme ultraviolet spectral region covering the M absorption edges of 3d ferromagnets is challenging due to the need for either a careful polarization analysis, which is complicated by a lack of efficient polarization analyzers, or scanning the angle of incidence in fine steps. Here, we propose and demonstrate a new technique to extract the complex resonant permittivity ϵ_{xy} simply by scanning the polarization angle of linearly polarized high harmonics to measure the magneto-optical asymmetry in reflection geometry. Because this technique is more practical and faster to experimentally implement than previous approaches, we can directly measure the full time evolution of $\epsilon_{xy}(t)$ during laser-induced demagnetization across the entire $M_{2,3}$ absorption edge of cobalt with femtosecond time resolution. We find that for polycrystalline Co films on an insulating substrate, the changes in ϵ_{xy} are uniform throughout the spectrum, to within our experimental precision. This result suggests that, in the regime of strong demagnetization, the ultrafast demagnetization response is primarily dominated by magnon generation. We estimate the contribution of exchange-splitting reduction to the ultrafast demagnetization process to be no more than 25%.

¹⁴ PACS numbers: 78.20.Ls 75.78.Jp 78.40.-q 78.47.-p

I. INTRODUCTION

The understanding of strongly coupled interactions in magnetic materials that occur in response to femtosecond laser excitation¹ is critical for advancing our fundamental knowledge of out-of-equilibrium materials systems; however, these are challenging to access both experimentally and theoretically. This knowledge is, moreover, important for utilizing the spin degree of freedom and for designing functional materials² and magnetic logic devices that can be controlled by ultrashort light pulses. Such spintronic devices could ultimately be used for fast and energy efficient spin-based logic^{3,4}. Because the characteristic spin dynamics of spin-flip processes^{5–8}, spin transport^{9–14}, and high energy spin-wave excitations^{15–17} occur on femtosecond to picosecond timescales, their investigation requires ultrashort pulses. To date, most measurements have used either femtosecond visible lasers or short wavelength synchrotron, free electron (FEL), and laser driven x-ray or extreme ultraviolet (EUV) light sources. Ultrafast laser probes have the advantage of very high time resolution and ease of access; however, visible lasers can only measure the net magnetic response of the entire system, with the exception of specific types of systems that contain both rare-earth and transition-metal elements and allow for element specificity in the visible range¹⁸. Short wavelength light can, in contrast, access the element-specific magnetic response in alloys and multilayers, without specific requirements for their composition, with the added advantage of broad energy bandwidth that enables measurements across the full M - and L -shell absorption edges that encode a magnetic state.

In previous work, tabletop high harmonic generation (HHG) has been used to explore the competition between spin-flip scattering and spin transport in the ultrafast demagnetization process^{13,19}. HHG sources were also recently used to indirectly extract the dynamic permittivity $\epsilon_{xy}(t)$ at two different times—during and after demagnetization and subsequent recovery of the magnetic state—by use of angle-resolved transverse magneto-optical Kerr effect (T-MOKE) measurements, in combination with *ab initio* calculations of the permittivity as a function of exchange splitting and magnon generation²⁰. However, the cumbersome need to scan both the time delay and the angle of incidence precluded the direct measurement of the dynamic magneto-optical permittivity $\epsilon_{xy}(t)$ as a continuous function of time, independent of theoretical modeling. Moreover, there are comparable challenges associated with all magneto-optical techniques at EUV and X-ray photon energies. Such challenges include the

need for a polarization state analysis in the case of longitudinal MOKE^{21–23} and Faraday
and Voigt rotation^{24–26}, scanning the angle of incidence for a measurement of X-ray mag-
netic circular dichroism (XMCD) in reflection²⁷, or for a polar MOKE measurement with an
out-of-plane magnetized sample^{21,22}, or XMCD in transmission geometry^{28,29}. As a result,
the transient $\epsilon_{xy}(t)$ during ultrafast demagnetization has not yet been measured.

Spin-resolved photoemission spectroscopy can also be used to investigate laser-induced
demagnetization dynamics^{30–32}. However, photoemission is sensitive only to the top surface
of the material. It is also difficult to use for the measurement of the band structure dynamics
across the entire Brillouin zone. In contrast, magneto-optical spectroscopy provides access
to the changes of the spin-polarized band structure across the entire Brillouin zone.

In this work, we present a new tabletop EUV magneto-optical technique that can be
used to directly measure the complex magneto-optical dielectric tensor element $\epsilon_{xy}(E, t)$ as
a function of both photon energy E and time t in order to capture its full dynamic evolution.
This new technique is therefore complementary to, and in some respects more powerful than,
existing approaches. The new technique makes use of a diagonal form of the magneto-optical
effect, or D-MOE, whereby the magnetization is obliquely oriented to the plane of incidence,
as illustrated in Fig. 1. D-MOE can be regarded as a superposition of two magneto-optical
geometries, T-MOKE^{21,22,33} and the lesser utilized longitudinal magneto-optical effect (L-
MOE)³⁴ which both give rise to a magnetization-dependent reflectivity change. In addition,
by scanning the polarization angle of the incident linearly polarized EUV light by rotating
the polarization of the driving laser light, we demonstrate that it is possible to uniquely
determine $\epsilon_{xy}(E)$, the full complex magneto-optical response. Moreover, the D-MOE ge-
ometry naturally lends itself for time-resolved studies for the extraction of $\epsilon_{xy}(E, t)$ as a
function of both time and photon energy. By use of the D-MOE geometry for the case of
ultrafast demagnetization with a polycrystalline Co film, we find that the fractional varia-
tion of $\epsilon_{xy}(E, t)$ over time is effectively independent of E across the entire M-edge to within
error bars. This result suggests that the dominant mechanism for ultrafast demagnetiza-
tion response is magnon generation when the magnetization is quenched by $\sim 42 \pm 5\%$ of
its saturation value, i.e., in the regime of strong demagnetization. We estimate an upper
limit of 25% for the contribution of the exchange splitting reduction of the dynamically
evolving band structure during ultrafast demagnetization. We note that these findings are
consistent within the experimental uncertainty with our previous work²⁰ that determined

the contributions of magnons and exchange splitting reduction at two specific times during the demagnetization process. Here, however, we access the full dynamic magnetic response as the material first demagnetizes and then begins to recover to its equilibrium state.

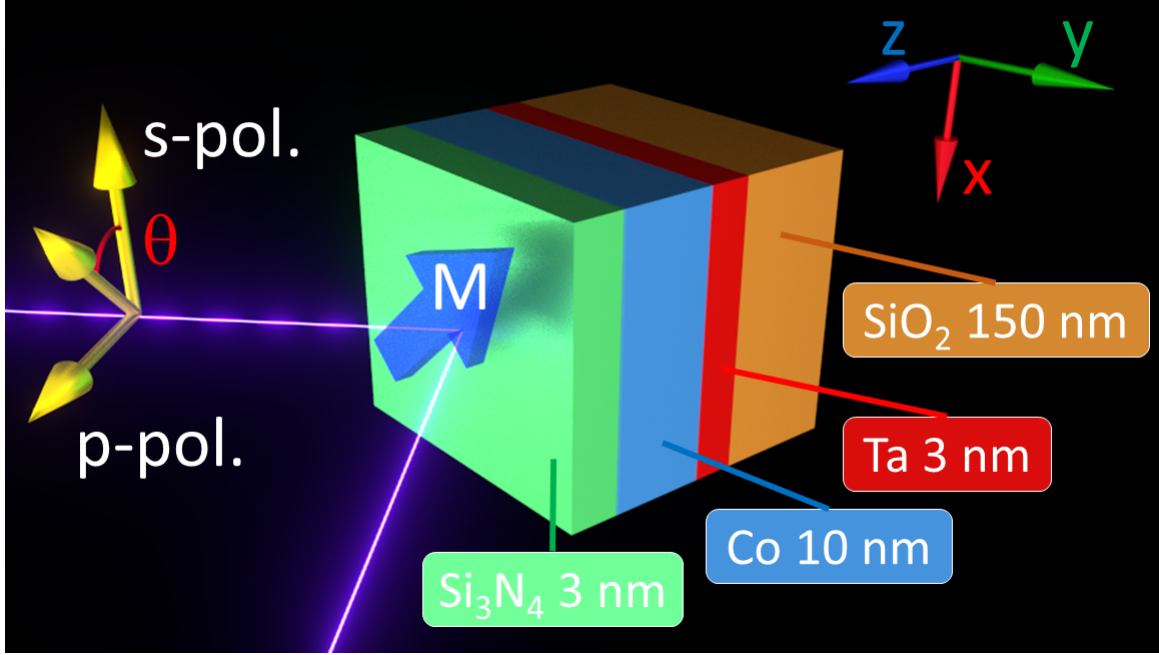


FIG. 1. Schematic of the diagonal magneto-optical effect (D-MOE) and the multilayer sample structure used for the static EUV D-MOE measurements. θ is the angle of the linearly polarized radiation relative to the s-polarization direction.

To demonstrate the time-resolved capability of D-MOE, we apply this technique to directly measure the static and dynamic $\epsilon_{xy}(E, t)$ at the $M_{2,3}$ absorption edge of 10 nm and 5 nm polycrystalline Co samples. The time step in our scan is 25 fs; a 28 times improvement over the previous work reported in Ref. 20. We validate our new D-MOE technique using three different approaches: first, we simulate T-MOKE and L-MOE signals on the basis of the dielectric constant values extracted by use of the D-MOE geometry. The simulations compare favorably with experimentally measured T-MOKE and L-MOE data. Second, we confirm that the real and imaginary parts of $\epsilon_{xy}(E)$ satisfy the Kramers-Kronig relations³⁵. Finally, we compare our measured ϵ_{xy} with theoretical calculations and also find a very good agreement.

In the following, we derive the D-MOE response at the boundary of two semi-infinite media and show that this effect can be used to uniquely solve for the real and imaginary

93 parts of ϵ_{xy} (see Appendix A). We then generalize this method to multilayer structures
 94 and also describe our experimental setup. We also present the static results for a cobalt
 95 sample and compare them with theoretical values. Finally, we implement D-MOE on a laser-
 96 excited sample. From the dynamic response, we find that there is a uniform reduction of the
 97 magnitude of ϵ_{xy} (cf. Ref. 20), within our error bars, suggesting that, for strong quenching,
 98 the demagnetization response is dominated primarily by ultrafast magnon generation with
 99 a possible smaller contribution from the dynamically evolving band structure (i.e., exchange
 100 splitting reduction).

101 **II. EXPERIMENTAL SETUP**

102 The experimental setup is shown in Fig. 2. Near-infrared (NIR) pulses at 790 nm with
 103 an energy of 1.2 mJ and at a 5 kHz repetition rate from an amplified ultrafast laser are
 104 focused into a hollow waveguide filled with He gas, where the EUV light is generated by the
 105 HHG process. We then direct the EUV probe beam onto the sample by use of a toroidal
 106 mirror, which focuses the probe beam onto an X-ray CCD camera after it impinges on a
 107 diffraction grating for spectral resolution. The sample itself is placed in front of a projection-
 108 field electromagnet that applies a magnetic field to the sample. The electromagnet can be
 109 rotated to magnetize the sample in the D-MOE geometry, which is at an angle to the
 110 plane of incidence of the EUV probe. The resultant reflectometry spectra measured in this
 111 geometry at different polarization angles of the linearly polarized probe are amenable to
 112 the unique determination of the magneto-optical dielectric constant – without any model-
 113 dependent constraints. Details on the mathematical analysis that proves this result can be
 114 found in Appendix A. To extract the spectrally resolved D-MOE, the reflected HHG beam
 115 is dispersed by a diffraction grating that is mounted in a conical configuration for higher
 116 efficiency³⁶. Aluminum foil filters of submicron thicknesses are used to reject any residual
 117 NIR light. For investigating laser-driven ultrafast demagnetization, we direct a fraction
 118 of the NIR light into a pump beam with a fluence of 2.7 mJ/cm² and p-polarization at
 119 the sample. The pump beam is collinear with the probe beam. Because the NIR light is
 120 generated by the same Ti:Sapphire laser, the laser pump pulses are intrinsically synchronized
 121 with the EUV probe pulses, with virtually no jitter. The polarization direction of the
 122 generated EUV light is identical to that of the driving laser due to the nature of the HHG

process^{37,38}. As such, the polarization of the EUV probe is controlled by use of a half-wave
plate to rotate the linear polarization angle of the driving laser beam.

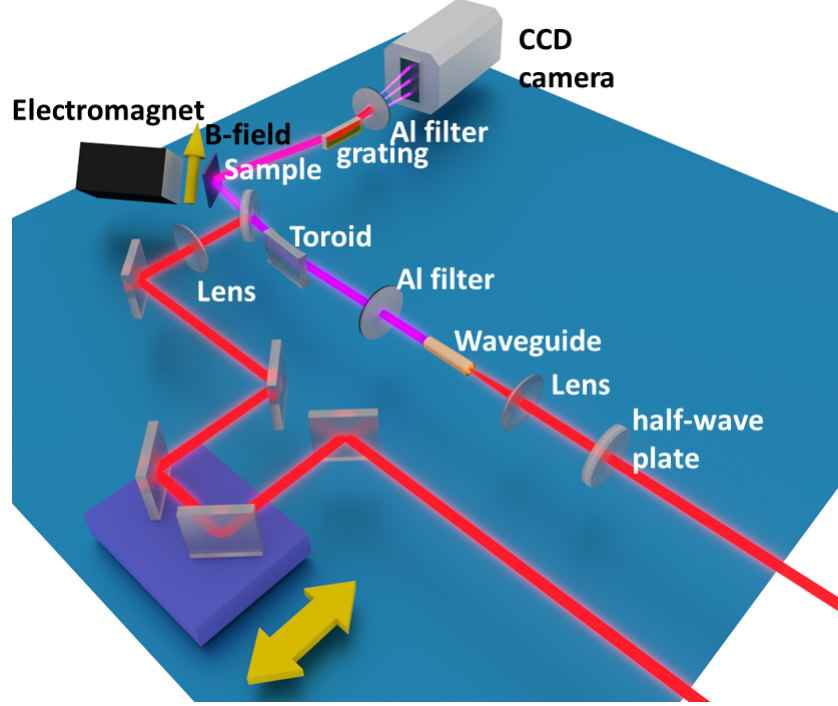


FIG. 2. Experimental setup to implement D-MOE. A half-wave plate is used to rotate the linear
polarization of the driving laser, and hence the polarization of the HHG beam.

III. RESULTS AND DISCUSSION

By use of the D-MOE geometry and a continuously rotated linear polarization of the
probe beam, we extracted the off-diagonal component of the dielectric tensor for two mul-
tilayer samples. The first sample, also shown in Fig. 1, is a multilayer stack consisting
of Si/SiO₂(150)/Ta(3)/Co(10)/Si₃N₄(3), where all thicknesses are reported in nanometers.
Static polarization scans on the Co multilayer stack were done at three different orientations
of the magnetization vector \vec{m} : transverse, longitudinal, and diagonal at 45° to the plane
of incidence of the EUV probe. Extraction of the ϵ_{xy} over the full energy range of the Co
M-edge follows the method described in Appendix A, and the diagonal components of the di-
electric constant used in the extraction of the ϵ_{xy} were taken from Ref. 39. The experimental
data for the three geometries, as well as the simulated magneto-optical signals based on the

138 ϵ_{xy} extracted from D-MOE, are shown in Fig. 3. The experimental points on the energy axis
 139 in Fig. 3 correspond to the harmonic peaks of the HHG probe spectrum. We can accurately

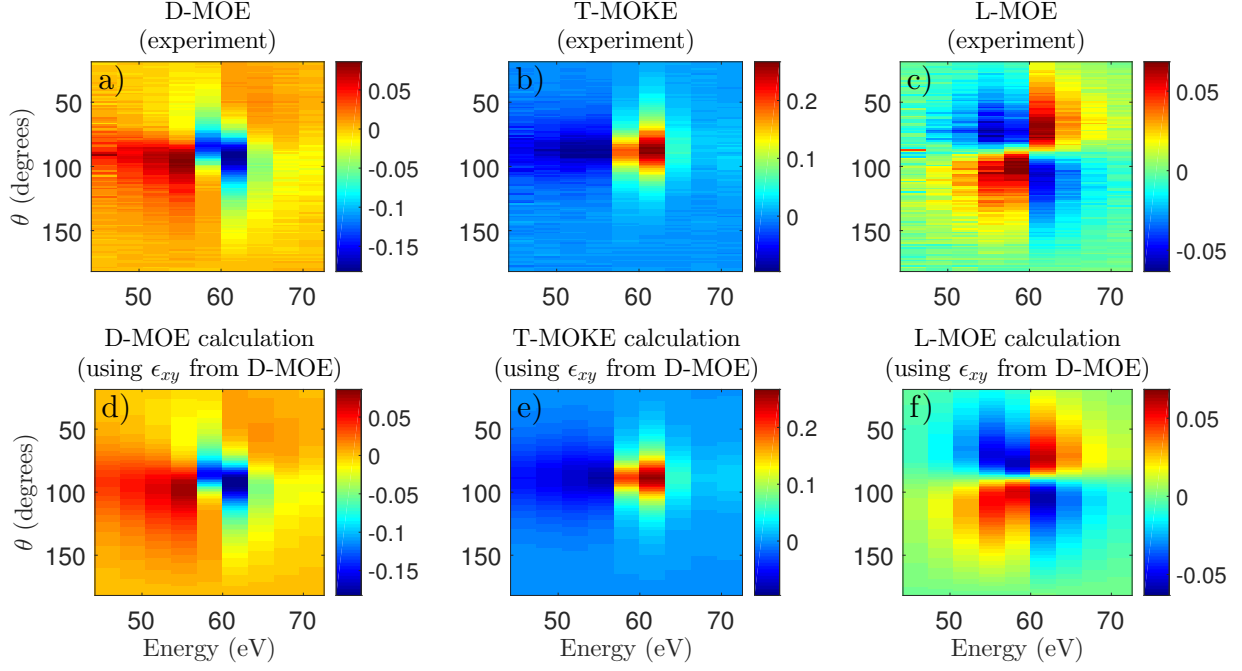


FIG. 3. Energy- and polarization angle-dependent magneto-optical spectra for the three orientations of the magnetization \vec{m} : D-MOE (a), T-MOKE (b), and L-MOE (c). The data are measured at the discrete harmonic peaks of the EUV probe spectrum. Polarization angle $\theta = 90^\circ$ corresponds to p-polarization. (d-f) are calculations for each geometry generated from the ϵ_{xy} that is extracted from fitted measurements in the D-MOE geometry.

140

141

142 calculate the magneto-optical reflectivity for both the T-MOKE and L-MOE geometries by
 143 use of the ϵ_{xy} extracted from the spectroscopic reflectivity data in the D-MOE geometry,
 144 as evidenced by the excellent agreement between the experimental and simulated data in
 145 Fig. 3b and 3e, as well as 3c and 3f. Conversely, we show in Fig. 4 that it is not possible
 146 to extract the correct general ϵ_{xy} from either the longitudinal or the transverse geometries
 147 by simply scanning the polarization, as discussed in Appendix A. This is because, in order
 148 to extract the full ϵ_{xy} , they require additional information, e.g. by scanning the angle of
 149 incidence in fine steps. Such an approach is possible, but very challenging for time-resolved
 150 measurements. An additional test of the fitted results is to verify if the real and imaginary
 152 parts of the extracted ϵ_{xy} are consistent with the Kramers-Kronig relations. As can be seen
 153 from Fig. 5, the real part of ϵ_{xy} obtained by applying a Kramers-Kronig transform to the

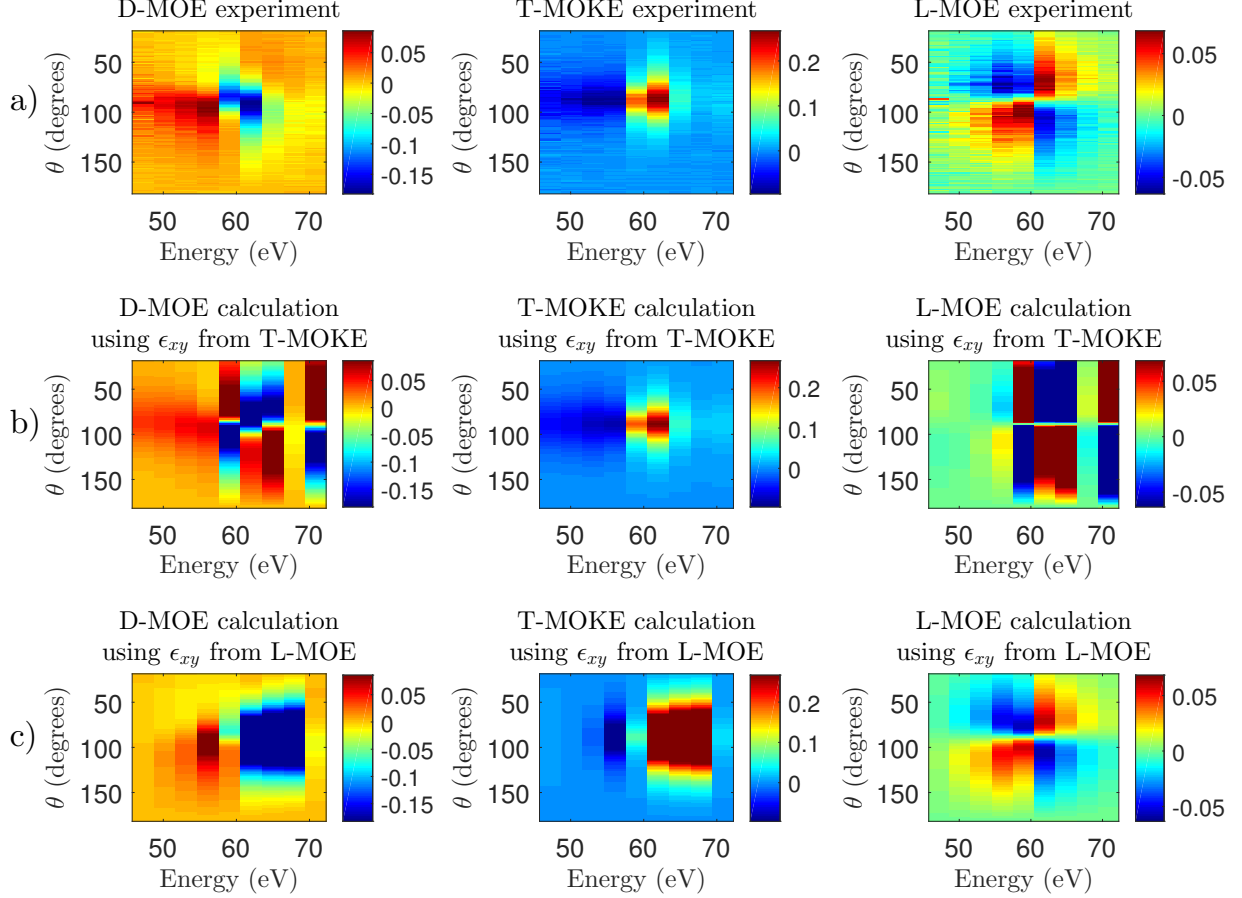


FIG. 4. (a) Polarization-resolved EUV magneto-optical signals with their reconstructions made using ϵ_{xy} extracted from (b) T-MOKE and (c) L-MOE. Note that the ϵ_{xy} extracted from the T-MOKE and L-MOE spectra are only capable of providing satisfactory reconstructions of their own signal, and not capable of reconstructing the signals in other geometries without scanning the angle of incidence. The same set of polarization angles was used for all the geometries shown in the figure.

interpolant of the imaginary part is consistent with the experimental values to within the measurement precision. The self-consistency of the measured ϵ_{xy} with the Kramers-Kronig relations is evidence in support of the D-MOE method. Furthermore, the extracted ϵ_{xy} spectra compare favorably with theoretical calculations (from Ref. 20), which are also shown in Fig. 5.

Having validated our D-MOE technique, we employed it in a stroboscopic pump-probe experiment to extract the dynamic evolution of $\epsilon_{xy}(E, t)$ on femtosecond time for the first time. For this purpose, we used the second sample, a 5 nm thick Co film grown on an

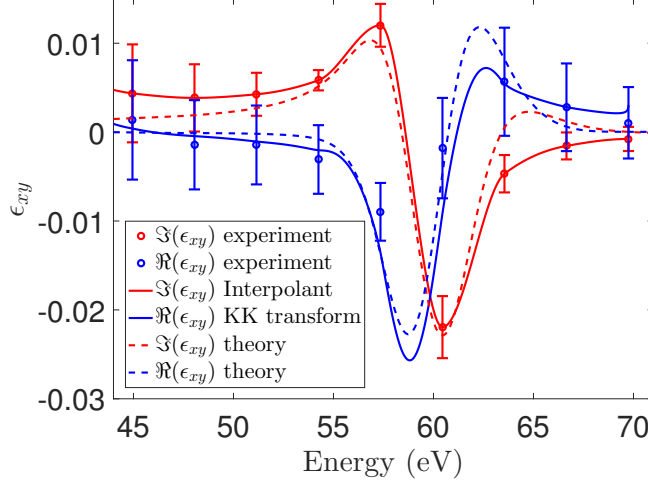


FIG. 5. Experimental ϵ_{xy} measured at the M -edge of Co, on a Si/SiO₂(150)/Co(5)/GeO₂(3) multilayer. Our data compare well with theoretical calculations²⁰, and the real and imaginary parts satisfy the Kramers-Kronig relations. The error bars are estimated based on the root-mean-square deviation of the HHG intensity (see Appendix C) for details.

insulating substrate without the presence of the seed layer, in order to isolate the dynamic changes in ϵ_{xy} as solely the result of local microscopic processes, as opposed to the generation of laser-induced spin currents^{9,13} which are non-local. We note that such extraction of the dynamic $\epsilon_{xy}(E, t)$ is only valid in the quasi-static approximation when changes in ϵ_{xy} are much slower compared to, in particular, the duration of the probe pulses. This is indeed the case since the characteristic time constant of ~ 230 fs for a dynamically evolving ϵ_{xy} is much longer than the duration of the sub-10 fs EUV probe pulses. Additionally, we constrain our analysis to timescales exceeding 100 fs—where we do not overlap with the 50-fs near-infrared pump pulse, and dynamic changes in ϵ_{xy} are large enough for us to draw definitive conclusions from the data given our experimental uncertainty.

We measured the dynamic magneto-optical response over a range of polarization angles from 30° to 150° with respect to s-polarization, as shown in Fig. 1. We used angle steps of 6.7° and time steps of 25 fs. The observed demagnetization response is shown in Fig. 6. It exhibits a fast reduction in magnetization, with an exponential time constant of ~ 233 fs, followed by a slower exponential recovery of ~ 2.4 ps. In the figure, two signals are compared: based on the raw data and that calculated from the dynamics of $\epsilon_{xy}(E, t)$. The raw data response (red circles) was obtained by averaging the signal over multiple discrete harmonic peaks and all

180 measured polarization angles. To improve the signal-to-noise ratio, integration was limited
 181 to angles and energies where the absolute value of the magneto-optical asymmetry exceeds
 182 0.12 before time-zero. The response based on the dynamics of $\epsilon_{xy}(E, t)$ (blue circles) was
 183 calculated from the integrated response of $\Im(\epsilon_{xy})$ over the energy range of 55 eV to 63 eV.
 184 The two methods agree well: the decay τ_D and recovery τ_R time constants of the standard
 185 double-exponential fit⁴⁰ are $\tau_D = 224 \pm 53$ fs and $\tau_R = 2302 \pm 623$ fs, based on the dynamics
 186 of $\epsilon_{xy}(E, t)$, and $\tau_D = 242 \pm 58$ fs and $\tau_R = 2417 \pm 686$ fs, based on the raw D-MOE data.

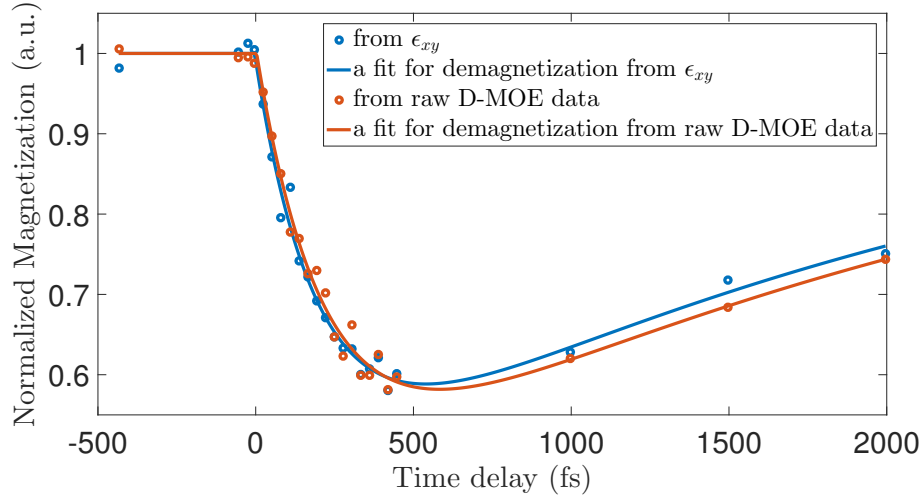


FIG. 6. Normalized laser-induced demagnetization response of a Si/SiO₂(150)/Co(5)/GeO₂(3)
 187 multilayer.

188
 189 From the polarization-resolved data, we extracted ϵ_{xy} at each time step in Fig. 6. The
 190 resulting evolution of the differential change $\Delta\epsilon_{xy}(E, t) = \epsilon_{xy}(E, t) - \epsilon_{xy}(E, t < 0)$ is shown in
 191 Figs. 7 (a) and (b) for both the real and imaginary parts, respectively. The data clearly show
 192 a transient decrease and recovery of ϵ_{xy} after laser excitation. The fundamental mechanisms
 193 underlying ultrafast laser-induced demagnetization have been intensely debated ever since
 194 the effect was first observed^{5,8,20,32,41–46}. Since non-local spin transport is minimized with the
 195 here-chosen sample geometry⁹, the remaining possible mechanisms are: longitudinal spin-
 196 flips, e.g. caused by electron-phonon scattering, that would eventually lead to a reduction
 197 of the exchange splitting^{5,7,47}, or demagnetization due to ultrafast non-equilibrium magnon
 198 generation^{8,15,17}. The former mechanism reduces the magnitude of the magnetization vector,
 199 while the latter preserves its magnitude but tilts the magnetization locally. Both types of
 200 excitation result in a reduced projection of the magnetization on a local z-axis, which can
 201

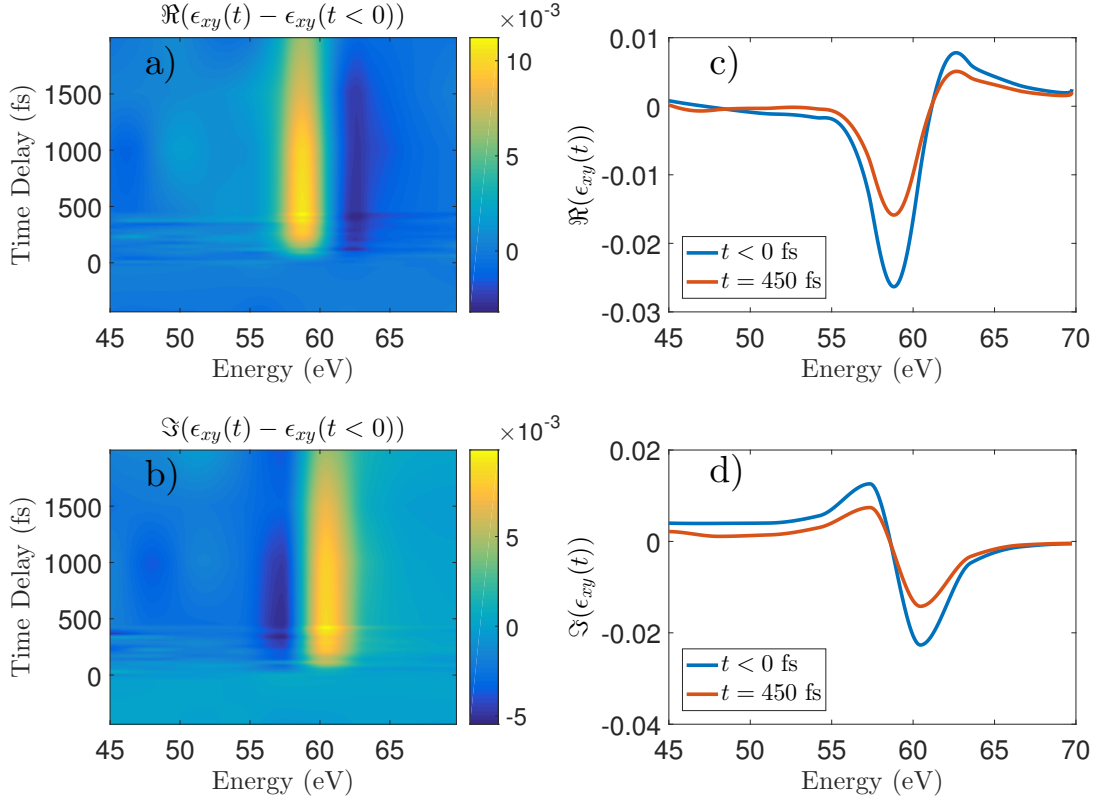


FIG. 7. Time-resolved differential changes in the real (a) and imaginary (b) parts of ϵ_{xy} with respect to the ground state at $t < 0$ fs and real (c) and imaginary (d) parts of ϵ_{xy} at $t < 0$ fs and $t = 450$ fs.

be measured by use of magneto-optical techniques. These mechanisms map onto the basic models of ferromagnetism in metallic systems: the Stoner picture⁴⁸, and the Heisenberg picture^{49,50}. As proposed in 1975 by Erskine and Stern when they first predicted X-ray magnetic circular dichroism (XMCD)⁵¹, these two theories of ferromagnetism each lead to specific spectral changes in ϵ_{xy} through which one could distinguish which mechanism was operative. The predicted effect of these two mechanisms on the time-resolved magneto-optical spectrum was confirmed recently by *ab initio* calculations; transverse spin excitations lead to a spectrally uniform, linear decrease of the amplitude of ϵ_{xy} (Ref. 20). Reducing or enhancing the Stoner exchange splitting, on the other hand, has been shown to lead to changes of peak positions in addition to non-linear changes in MOKE peak amplitudes^{20,52}.

As shown in Fig. 8, to within the error bars of our measurement, the change in ϵ_{xy} after laser excitation appears uniform across the entire M -edge between 45 eV and 70 eV. This is consistent with the predicted behavior for ultrafast magnon generation. However,

215 a nonzero reduction of the exchange-splitting cannot be excluded, given the measurement
 216 precision. To illustrate this, in Fig. 8b we plot three theoretically calculated $\Im(\epsilon_{xy})$ curves—
 217 one with an unperturbed exchange splitting and two with a quenched exchange leading to
 218 a reduction of the magnitude of the magnetic moment from $1.63 \mu_B$ to $1.42 \mu_B$ and to
 219 $0.97 \mu_B$ —along with the measured $\Im(\epsilon_{xy})$ at 450 fs. Notably, the theoretical curves also

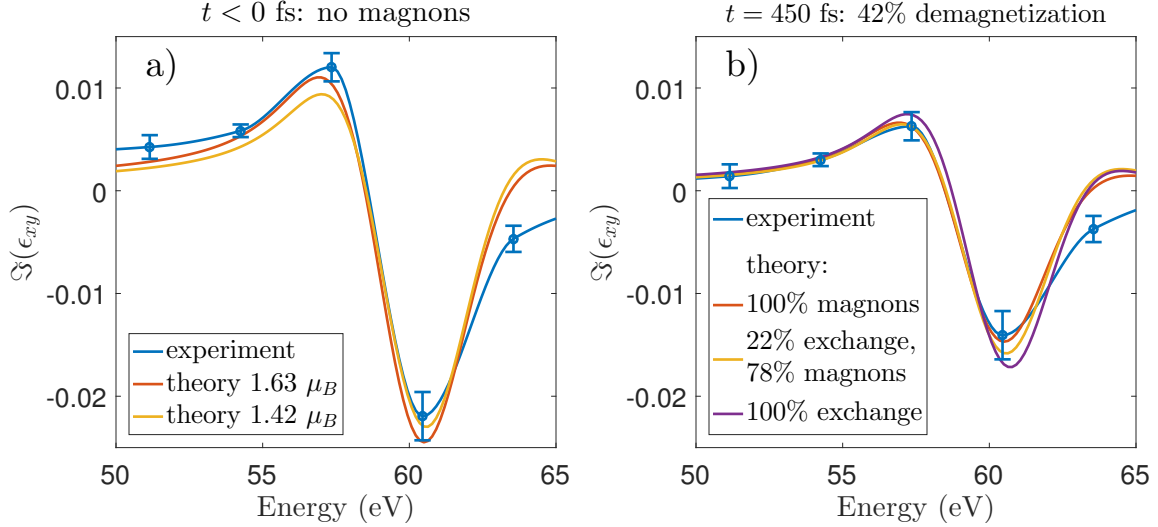


FIG. 8. Comparison of the experimental ϵ_{xy} with the theoretical values calculated *ab initio* for the
 ground state as well as excited states of cobalt with reduced values of exchange splitting. a) $t \leq 0$ fs
 where theory does not include any magnon excitation. b) $t = 450$ fs where the theory curves have
 been scaled as if demagnetization was entirely due to magnon generation (red curve), and also when
 $\sim 3/4$ and $\sim 1/4$ of the total 42% demagnetization were due to magnons and exchange splitting
 reduction, respectively (yellow curve), and when the demagnetization was entirely due to exchange
 splitting reduction (purple curve). Since the difference between the theoretical ϵ_{xy} for the cases
 of 78% and 100% magnon contribution (yellow and red curves) to the total demagnetization lies
 within the experimental error bars (see Appendix C), while it is outside of the errorbars for the
 case of 100% exchange reduction contribution (purple curve), we conclude that exchange splitting
 reduction plays a lesser role in the magnetization reduction, contributing at most $\sim 1/4$ of the
 observed signal.

220

221

222 take into account the respective magnon contributions such that the net demagnetization
 223 of all three curves is at the experimentally measured value of 42%, i.e. the projection of
 224 the magnetic moment on the local z -axis is reduced from $1.63 \mu_B$ to $0.97 \mu_B$, for the three

cases. The demagnetization is either entirely due to magnons (red curve in Fig. 8b) or to exchange splitting reduction (purple curve in Fig. 8b), or magnons contribute $\sim 3/4$ to the signal, while exchange reduction contributes $\sim 1/4$ of the signal (yellow curve in Fig. 8b). As can be seen from the figure, the theoretical ϵ_{xy} have different spectral shapes which confirms the prediction made by Erskine and Stern⁵¹. For details on the theoretical ϵ_{xy} for various values of exchange splitting, see Appendix D. An ϵ_{xy} that results solely from a reduced exchange splitting does not fit the experimental data well, and thus we exclude the collapse of exchange splitting as the single driver of ultrafast demagnetization. The biggest change occurs around 60.5 eV. However, for the yellow curve in Fig. 8b, this change is still within the experimental error. This puts an upper limit on the possible contribution of the exchange splitting reduction to the net demagnetization: to within the estimated measurement precision for the magnitude of ϵ_{xy} of $\sim 25\%$ at 60.5 eV, the upper limit for the relative contribution of exchange-splitting-reduction is also $\sim 25\%$. Conversely, no less than $\sim 75\%$ of the laser-induced demagnetization is dominated by ultrafast magnon generation. This result is consistent with both our previous work²⁰, and with recent transient spin-resolved photoemission measurements³².

We would like to note that, because of the inherent experimental uncertainty, our new D-MOE technique yields useful information when transient changes in ϵ_{xy} are sufficiently large. On sub-100 fs timescales, such changes are subtle, and further work is needed to determine the microscopic mechanisms at work on such fast times. It has been proposed that the spin-orbit interaction^{53,54} plays an important role in the initial demagnetization that takes place in the spin-polarized valence states. The spin-orbit interaction in the valence band, which is much smaller than that in the semi-core states, can lead through electron-phonon scattering to longitudinal spin flips that cause a reduction of the exchange splitting⁵.

IV. SUMMARY

We found that for a Co multilayer grown on an insulating substrate, the changes in ϵ_{xy} caused by ultrafast demagnetization were uniform across the M -edge, within the experimental uncertainty. This finding suggests that laser-induced demagnetization, in the limit of strong quenching, predominantly results from ultrafast non-equilibrium magnon generation with a possible, yet quite smaller contribution from a dynamically reduced exchange

splitting. Our measurements thus provide a strong support of ultrafast magnon generation⁸ as a dominant mechanism of laser-induced demagnetization on sub-picosecond timescales, in contrast to a quenching of the exchange splitting^{5,7} caused by fast spin-flip scattering. Further work is needed to determine the cause of the ultrafast magnon generation on sub-100 fs timescales, and longitudinal spin flips and the spin-orbit interaction^{53,54} seem to be promising candidates for that role. To obtain the spectra utilized in this study, we demonstrated a new method for efficient extraction of the off-diagonal dielectric tensor component across the M -shell absorption edge of a magnetic material in a reflection geometry by measuring the magneto-optical response of a multilayer sample at different polarization angles of the probe beam from a laser-driven tabletop HHG source. This method is very well suited for measuring the full transient magneto-optical response to an intense near-infrared laser pulse with femtosecond time resolution. In the future, we expect that D-MOE measurements can be combined with density functional theory (DFT) calculations to map the full dynamic band structure of a demagnetizing magnetic material.

ACKNOWLEDGMENTS

This work was done at JILA; H.C.K. and M.M.M. acknowledge support from the Department of Energy (DOE) Office of Basic Energy Sciences X-Ray Scattering Program Award No. DE-SC0002002 and a Gordon and Betty Moore Foundation EPiQS Award through Grant No. GBMF4538. P.M.O. acknowledges financial support from the Swedish Research Council (VR) and the Knut and Alice Wallenberg Foundation (Grant No. 2015.0060). D.L. acknowledges support by the European Regional Development Fund in the IT4Innovations national supercomputing center Path to Exascale project, No. CZ.02.1.01/0.0/0.0/16_013/0001791 within the Operational Programme Research, Development and Education and grant No. 17-27790S of the Czech Science Foundation. The authors acknowledge fruitful discussions with Karel Carva, Emrah Turgut, and Patrik Grychtol.

Appendix A: Two-axis magneto-optical effect D-MOE

We first consider D-MOE at an interface as shown in Fig. 1. In the s- and p-polarization basis (E_s, E_p) , the incident electric field \vec{E}_i , i.e., the time- and space-independent part of

the plane-wave radiation, can be written as

$$\vec{E}_i = \begin{pmatrix} E_s \\ E_p \end{pmatrix} = \begin{pmatrix} \cos \theta \\ \sin \theta \end{pmatrix} E_0, \quad (\text{A1})$$

where E_0 is the amplitude of the incoming electric field vector; in the following, we shall set E_0 to 1. θ is the angle of the linearly polarized radiation relative to the s-polarization direction. The reflected field \vec{E}_r is related to the incident field through the 2x2 bulk Fresnel reflection matrix $\hat{\mathbf{r}}$ as

$$\vec{E}_r = \hat{\mathbf{r}} \vec{E}_i = \hat{\mathbf{r}} \begin{pmatrix} \cos \theta \\ \sin \theta \end{pmatrix}. \quad (\text{A2})$$

This matrix depends on the magnetization direction \vec{m} (see, e.g. Refs. 55 and 35); when \vec{m} lies in the (x, y) plane, i.e., $\vec{m} = (m_x, m_y, 0)$, as in Fig. 1, it can be expressed to first order in the magneto-optical Voigt constant $Q = i\epsilon_{xy}/\epsilon_{xx}$, as

$$\hat{\mathbf{r}}(\vec{m}) = \begin{pmatrix} r_{ss} & r_{sp} \\ r_{ps} & r_{pp} \end{pmatrix} \simeq \begin{pmatrix} r_{ss}^{(0)} & r_{sp}^{(1)} m_y Q \\ -r_{sp}^{(1)} m_y Q & r_{pp}^{(0)} + r_{pp}^{(1)} m_x Q \end{pmatrix}, \quad (\text{A3})$$

where the superscripts (0) and (1) indicate the coefficients in terms independent of and linear in Q , respectively. Note that $r_{ss}^{(0)} \equiv r_{ss}$. To quantify the difference in reflectivity from the boundary for two opposite directions of \vec{m} , we define a quantity called the magneto-optical asymmetry A as the normalized reflectivity difference

$$A = \frac{R_+ - R_-}{R_+ + R_-}, \quad (\text{A4})$$

where $R_{\pm} = |\vec{E}_r(\pm\vec{m})|^2$. From equations (A2), (A3), and (A4), one can show that the asymmetry for a sample magnetized in-plane, with components along the x and y axes, to a first order in Q , is

$$A = \frac{m_y \sin 2\theta \Re \left((r_{ss} - r_{pp}^{(0)*} r_{sp}^{(1)} Q) \right) - m_x (1 - \cos 2\theta) \Re \left(r_{pp}^{(0)*} r_{pp}^{(1)} Q \right)}{|r_{pp}^{(0)}|^2 \sin^2 \theta + |r_{ss}|^2 \cos^2 \theta}, \quad (\text{A5})$$

where \Re is the real part of an expression.

We now consider special cases of expression (A5) for the transverse $\vec{m} = (1, 0, 0)$, longitudinal $\vec{m} = (0, 1, 0)$, and mixed $\vec{m} = \frac{1}{\sqrt{2}}(1, 1, 0)$ magnetization directions. For the transverse configuration, we obtain

$$A_T := A(m_x = -1; m_y = 0) = \frac{(1 - \cos 2\theta) \Re \left(r_{pp}^{(0)*} r_{pp}^{(1)} Q \right)}{|r_{pp}^{(0)}|^2 \sin^2 \theta + |r_{ss}|^2 \cos^2 \theta}, \quad (\text{A6})$$

which matches with the well-known T-MOKE asymmetry⁵⁶ which is normally defined for p-polarized light, i.e., for $\theta = \pi/2$. We also recover the result for the L-MOE in the longitudinal configuration³⁴,

$$A_L := A(m_x = 0; m_y = 1) = \frac{\sin 2\theta \Re \left((r_{ss} - r_{pp}^{(0)})^* r_{sp}^{(1)} Q \right)}{|r_{pp}^{(0)}|^2 \sin^2 \theta + |r_{ss}|^2 \cos^2 \theta}. \quad (\text{A7})$$

For L-MOE, note that the reflectivity change is zero for the case of s- or p-polarized light, i.e., $\theta = 0, \pi/2$, and thus an incident beam with a mixed polarization state is needed to observe a magnetization-dependent reflectivity change.

Next, we show that it is possible to obtain a unique solution for the complex Q in the D-MOE geometry, while also demonstrating that it is impossible to use longitudinal or transverse geometries for this purpose. We choose a symmetric configuration with the magnetization set at 45° with respect to the scattering plane, i.e., $\vec{m} = \frac{1}{\sqrt{2}}(1, 1, 0)$. We would like to emphasize that the results would still hold for any other configuration as well, as long as both m_x and m_y magnetization components are non-zero. For our case, after expanding the real part in (A5) as $\Re(z) = \frac{1}{2}(z + z^*)$, the magneto-optical asymmetry reads

$$A_D := A \left(m_x = -\frac{1}{\sqrt{2}}; m_y = \frac{1}{\sqrt{2}} \right) = F_D(\theta)Q + F_D^*(\theta)Q^*, \quad (\text{A8})$$

where we defined the complex factor $F_D(\theta)$ as

$$F_D(\theta) = \frac{\sin 2\theta (r_{ss} - r_{pp}^{(0)})^* r_{sp}^{(1)} + (1 - \cos 2\theta) r_{pp}^{(0)*} r_{pp}^{(1)}}{2\sqrt{2} \left(|r_{pp}^{(0)}|^2 \sin^2 \theta + |r_{ss}|^2 \cos^2 \theta \right)}. \quad (\text{A9})$$

To exemplify how this is different from A_T and A_L , we rewrite A_T and A_L in a similar form

$$A_T = F_T(\theta)Q + F_T^*(\theta)Q^* \equiv f_T(\theta) \left(r_{pp}^{(0)*} r_{pp}^{(1)} Q + r_{pp}^{(0)} r_{pp}^{(1)*} Q^* \right), \quad (\text{A10})$$

317

$$A_L = F_L(\theta)Q + F_L^*(\theta)Q^* \equiv f_L(\theta) \left((r_{ss} - r_{pp}^{(0)})^* r_{sp}^{(1)} Q + (r_{ss} - r_{pp}^{(0)}) r_{sp}^{(1)*} Q^* \right), \quad (\text{A11})$$

with $f_T(\theta)$ and $f_L(\theta)$ (as well as $F_T(\theta)$ and $F_L(\theta)$) defined as

$$f_T(\theta) \equiv \frac{F_T(\theta)}{r_{pp}^{(0)*} r_{pp}^{(1)}} = \frac{(1 - \cos 2\theta)}{2 \left(|r_{pp}^{(0)}|^2 \sin^2 \theta + |r_{ss}|^2 \cos^2 \theta \right)}, \quad (\text{A12})$$

319

$$f_L(\theta) \equiv \frac{F_L(\theta)}{(r_{ss} - r_{pp}^{(0)})^* r_{sp}^{(1)}} = \frac{\sin 2\theta}{2 \left(|r_{pp}^{(0)}|^2 \sin^2 \theta + |r_{ss}|^2 \cos^2 \theta \right)}. \quad (\text{A13})$$

It is important to note that the prefactors $f_T(\theta)$ and $f_L(\theta)$, which contain the angular dependence, are purely real, while $F_D(\theta)$ has a complex dependence on θ . In order to solve for Q and Q^* and thus find the real and imaginary parts of Q , we need two linearly independent equations. We can obtain those by measuring the magneto-optical asymmetry at two different polarization angles θ_1 and θ_2 . This leads to a system of equations that can be written in a matrix form as

$$\begin{pmatrix} a_x & b_x \\ c_x & d_x \end{pmatrix} \begin{pmatrix} Q \\ Q^* \end{pmatrix} = \begin{pmatrix} A_x(\theta_1) \\ A_x(\theta_2) \end{pmatrix}, \quad (\text{A14})$$

where the subscript $x = T, L$ or D . We write explicitly the system matrix $\mathbf{\Lambda}_x$ for the transverse, longitudinal, and diagonal cases using equations (A10), (A11), and (A8), respectively

$$\mathbf{\Lambda}_T := \begin{pmatrix} a_T & b_T \\ c_T & d_T \end{pmatrix} = \begin{pmatrix} f_T(\theta_1) r_{pp}^{(0)*} r_{pp}^{(1)} & f_T(\theta_1) r_{pp}^{(0)} r_{pp}^{(1)*} \\ f_T(\theta_2) r_{pp}^{(0)*} r_{pp}^{(1)} & f_T(\theta_2) r_{pp}^{(0)} r_{pp}^{(1)*} \end{pmatrix}, \quad (\text{A15})$$

$$\mathbf{\Lambda}_L := \begin{pmatrix} a_L & b_L \\ c_L & d_L \end{pmatrix} = \begin{pmatrix} f_L(\theta_1) (r_{ss} - r_{pp}^{(0)*} r_{sp}^{(1)}) & f_L(\theta_1) (r_{ss} - r_{pp}^{(0)} r_{sp}^{(1)*}) \\ f_L(\theta_2) (r_{ss} - r_{pp}^{(0)*} r_{sp}^{(1)}) & f_L(\theta_2) (r_{ss} - r_{pp}^{(0)} r_{sp}^{(1)*}) \end{pmatrix}, \quad (\text{A16})$$

$$\mathbf{\Lambda}_D := \begin{pmatrix} a_D & b_D \\ c_D & d_D \end{pmatrix} = \begin{pmatrix} F_D(\theta_1) & F_D^*(\theta_1) \\ F_D(\theta_2) & F_D^*(\theta_2) \end{pmatrix}. \quad (\text{A17})$$

In order for a linear system with a non-zero right-hand side to have a unique solution, the determinant of the system matrix must be non-zero. For the matrices (A15), (A16), and (A17), the determinants are

$$\det \mathbf{\Lambda}_T = f_T(\theta_1) f_T(\theta_2) \left(|r_{pp}^{(0)}|^2 |r_{pp}^{(1)}|^2 - |r_{pp}^{(0)*}|^2 |r_{pp}^{(1)*}|^2 \right) \equiv 0, \quad (\text{A18})$$

$$\det \mathbf{\Lambda}_L = f_L(\theta_1) f_L(\theta_2) \left(|r_{ss} - r_{pp}^{(0)}|^2 |r_{sp}^{(1)}|^2 - |r_{ss} - r_{pp}^{(0)*}|^2 |r_{sp}^{(1)*}|^2 \right) \equiv 0, \quad (\text{A19})$$

$$\det \mathbf{\Lambda}_D = F_D(\theta_1) F_D^*(\theta_2) - F_D^*(\theta_1) F_D(\theta_2) \neq 0. \quad (\text{A20})$$

The determinants for the transverse and longitudinal magnetization geometries vanish, while the non-zero determinant is possible only in the diagonal two-axis geometry under the condition that $\cos(\theta_1) \sin(\theta_2) \neq \sin(\theta_1) \cos(\theta_2)$ which is fulfilled when $\theta_{1,2} \neq 0$ and $\theta_1 \neq \theta_2$. The latter geometry can thus be used to extract the full complex Q , and hence ϵ_{xy} , by measuring the D-MOE response at different polarization angles.

For the case of thin film samples with a multilayer structure, such as in Fig. 1, interference effects must be taken into account in order to accurately extract ϵ_{xy} . To do this, we compute

the magneto-optical reflectivity of the sample for opposite directions of \vec{m} by use of the multilayer modeling formalism of Zak *et al.*⁵⁷. From the computed reflectivity, we then calculate the D-MOE asymmetry to compare with the data. Because this method does not utilize an analytic expression, extraction starts with a guess solution for ϵ_{xy} that is then iteratively adjusted until the calculated polarization angle-dependent magneto-optical asymmetry fits the experimentally measured signal to within the experimental uncertainties. As we show in section III, the multilayer fitting procedure is robust for the particular sample considered.

Appendix B: Effect of optical elements on the magneto-optical signal

Here, we verify that the toroidal mirror and the diffraction grating do not affect our measurements. The former could potentially introduce ellipticity into the probe beam, while the latter could have varying diffraction efficiencies for different polarization directions which could distort the measured magneto-optical response of the sample. While the reflectance of the mirror does depend on the polarization of the incident light, it does not affect our measurements since we are interested in the relative change of the magneto-optical reflectivity upon a full reversal of the sample's magnetization and not in its absolute magnitude. For a toroidal mirror consisting of a Pyrex glass substrate coated with 100 nm of B_4C , we calculate for the S_3 Stokes parameter of the reflected beam normalized by the total intensity, a value $S_3 \leq 0.11$ ($S_3 = 0$ for linear and $S_3 = \pm 1$ for circular polarization) at a 6° grazing incidence. This means that the electric field on the minor semi-axis of the polarization ellipse is less than 0.055 of the field on the major semi-axis. Such a small ellipticity can be neglected for our purposes.

Next, we consider the effect of the diffraction grating on the measured signal. While the absolute diffraction efficiency does change as we rotate the polarization of the EUV probe, this change is not of concern for us because our measurements are differential. However, the polarization state of the light reflected from the sample could change due to the magneto-optical rotation. Generally speaking, for the two opposite magnetization directions of the sample $\pm\vec{m}$, the polarization states of the reflected light are different. This could result in different diffraction efficiencies for $+\vec{m}$ and $-\vec{m}$, which would distort the signal. We confirm that this effect is negligible by performing a rigorous coupled wave analysis (RCWA)^{58–60}

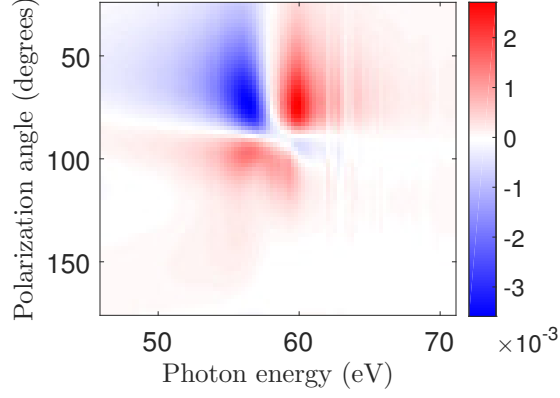


FIG. 9. Influence of the spectrometer diffraction grating on the measured D-MOE asymmetry: difference in diffraction efficiencies of the light reflected from a cobalt multilayer Si/SiO₂(150)/Ta(3)/Co(10)/Si₃N₄(3) for the two opposite magnetization directions $\pm\vec{m}$. A sawtooth grating made of Zerodur glass and coated with 30 nm of B₄C with a period of 2 μm and a blaze angle of 4.7° was set in a conical configuration at a 5° grazing incidence, and the grating vector was turned by 2° from the normal to the plane of incidence. These data show that the maximum difference in diffraction efficiency does not exceed 0.35% for different incident polarization angles.

of the grating response to the light reflected from the sample. The results of this analysis are shown in Fig. 9. First, we calculate magneto-optical reflections from the sample using a multilayer approach proposed by Zak *et al.*⁵⁷ Based on the calculated reflections, we determine the polarization state of the reflected light and use it as an input for the RCWA model. We find that, for our conditions, a change in diffraction efficiency for the opposite magnetization directions does not exceed 0.35%, as can be seen from Fig. 9. Such a small change can be safely neglected.

Appendix C: Estimation of the uncertainty of ϵ_{xy}

Because ϵ_{xy} is extracted by use of a fitting procedure based on the multilayer formalism⁵⁷ rather than an analytic expression, care must be taken in propagating the errors caused by intensity fluctuations of the EUV probe. This includes several steps. First, we calculate an

384 uncertainty ΔA in the magneto-optical asymmetry defined by equation (A4)

$$\Delta A = \sqrt{\left(\frac{\partial A}{\partial R_+} \Delta R_+\right)^2 + \left(\frac{\partial A}{\partial R_-} \Delta R_-\right)^2} = \frac{2\sqrt{R_-^2 \Delta R_+^2 + R_+^2 \Delta R_-^2}}{(R_+ + R_-)^2}, \quad (\text{C1})$$

385 where ΔR_+ and ΔR_- are the root-mean-square deviations of the reflected intensities for the
 386 positive and negative magnetization directions of the sample, respectively. These quantities
 387 were measured at each harmonic peak of the HHG spectrum, and they characterize the
 388 stability of the source. In the experiment, the asymmetry was averaged over 100 exposures
 389 of the X-ray CCD camera, but only the averaged values were recorded in order to improve
 390 the speed of data acquisition. We simulate a normally distributed random set of asymmetries
 391 with the calculated standard deviation ΔA and a mean A equal to the measured asymmetry.
 392 For each asymmetry from the set, we extract ϵ_{xy} and thus obtain a set of ϵ_{xy} values for which
 393 we calculate the root-mean-square deviations at each energy point. This procedure gives us
 394 the error bars displayed in Figures 5 and 8.

395 **Appendix D: *Ab initio* calculation of ϵ_{xy}**

396 We adopt the same approach for the calculation of ϵ_{xy} as in Ref. 20. In order to account
 397 for the lifetime broadening of the transition from the $3p$ orbital to the conduction band
 398 and for the exact energy of the $3p$ orbital, we convolve the theoretical ϵ_{xy} with a gaussian
 399 function and apply a small shift in energy, to align the theoretical $3p$ -semicore level positions
 400 with the measurements. The width and the amplitude of the gaussian as well as the value of
 401 the energy shift are found by a least square fitting of the ground-state theoretical ϵ_{xy} to the
 402 static experimental data. The parameters found from the fit are then applied to the excited
 403 state values of ϵ_{xy} which are compared to the experimental data at 450 fs in Fig. 8. In Fig.
 405 10, we are showing the *ab initio* calculated ϵ_{xy} for various values of exchange splitting and
 406 magnon excitation without applying any energy shifts or gaussian broadening.

407 All the curves shown in the figure correspond to a reduction of the z -axis projection of the
 408 magnetic moment from $1.63 \mu_B$ to $0.97 \mu_B$, i.e., to 42% demagnetization, and clearly show
 409 variations in the spectral shape and energy shifts of the ϵ_{xy} spectrum for reduced values of
 410 exchange splitting. This calculation confirms the original prediction made by Erskine and

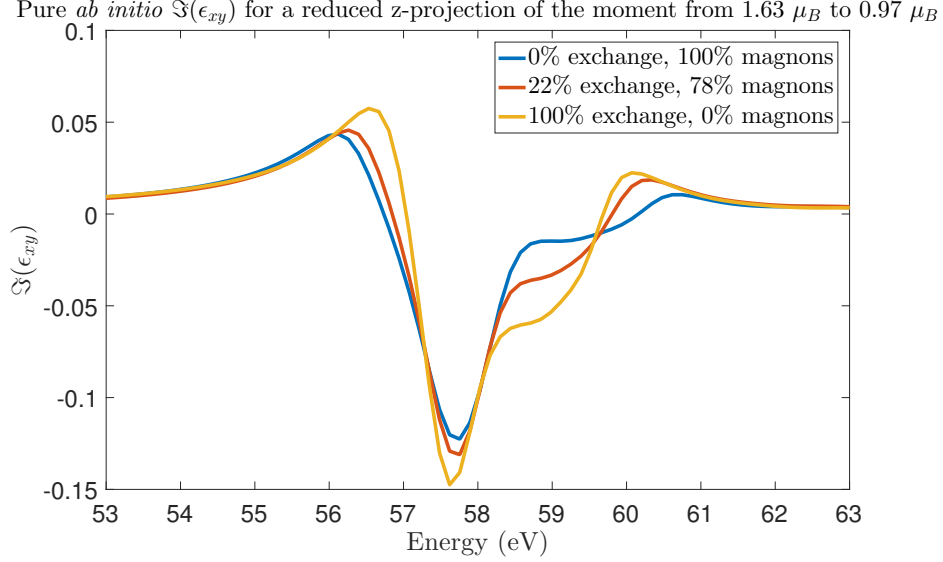


FIG. 10. *Ab initio* calculated ϵ_{xy} of Co without gaussian broadening and energy shifts for different contributions of the exchange splitting reduction and magnon excitation. The total demagnetization is 42% for each of the calculated ϵ_{xy} spectra.

411 Stern⁵¹.

412 * dmitriy.zusin@colorado.edu

413 ¹ E. Beaupaire, J.-C. Merle, A. Daunois, and J.-Y. Bigot, Physical Review Letters **76**, 4250
414 (1996).

415 ² S. Mangin, M. Gottwald, C.-H. Lambert, D. Steil, V. Uhlř, L. Pang, M. Hehn, S. Alebrand,
416 M. Cinchetti, G. Malinowski, Y. Fainman, M. Aeschlimann, and E. E. Fullerton, Nature Ma-
417 terials **13**, 286 (2014).

418 ³ S. A. Wolf, D. D. Awschalom, R. A. Buhrman, J. M. Daughton, S. v. Molnár, M. L. Roukes,
419 A. Y. Chtchelkanova, and D. M. Treger, Science **294**, 1488 (2001).

420 ⁴ A. V. Chumak, V. I. Vasyuchka, A. A. Serga, and B. Hillebrands, Nature Physics **11**, 453
421 (2015).

422 ⁵ B. Koopmans, G. Malinowski, F. Dalla Longa, D. Steiauf, M. Föhnle, T. Roth, M. Cinchetti,
423 and M. Aeschlimann, Nature Materials **9**, 259 (2010).

424 ⁶ M. Cinchetti, M. Sánchez Albaneda, D. Hoffmann, T. Roth, J.-P. Wüstenberg, M. Krauß,

- 425 O. Andreyev, H. C. Schneider, M. Bauer, and M. Aeschlimann, Physical Review Letters **97**,
426 177201 (2006).
- 427 ⁷ B. Y. Mueller, A. Baral, S. Vollmar, M. Cinchetti, M. Aeschlimann, H. C. Schneider, and
428 B. Rethfeld, Physical Review Letters **111**, 167204 (2013).
- 429 ⁸ E. Carpene, E. Mancini, C. Dallera, M. Brenna, E. Puppini, and S. De Silvestri, Physical Review
430 B **78**, 174422 (2008).
- 431 ⁹ M. Battiato, K. Carva, and P. M. Oppeneer, Physical Review Letters **105**, 027203 (2010).
- 432 ¹⁰ J. Wieczorek, A. Eschenlohr, B. Weidtmann, M. Rösner, N. Bergeard, A. Tarasevitch, T. O.
433 Wehling, and U. Bovensiepen, Physical Review B **92**, 174410 (2015).
- 434 ¹¹ G. Malinowski, F. Dalla Longa, J. H. H. Rietjens, P. V. Paluskar, R. Huijink, H. J. M. Swagten,
435 and B. Koopmans, Nature Physics **4**, 855 (2008).
- 436 ¹² A. Melnikov, I. Razdolski, T. O. Wehling, E. T. Papaioannou, V. Roddatis, P. Fumagalli,
437 O. Aktsipetrov, A. I. Lichtenstein, and U. Bovensiepen, Physical Review Letters **107**, 076601
438 (2011).
- 439 ¹³ D. Rudolf, C. La-O-Vorakiat, M. Battiato, R. Adam, J. M. Shaw, E. Turgut, P. Maldonado,
440 S. Mathias, P. Grychtol, H. T. Nembach, T. J. Silva, M. Aeschlimann, H. C. Kapteyn, M. M.
441 Murnane, C. M. Schneider, and P. M. Oppeneer, Nature Communications **3**, 1037 (2012).
- 442 ¹⁴ S. Mathias, C. La-O-Vorakiat, P. Grychtol, P. Granitzka, E. Turgut, J. M. Shaw, R. Adam,
443 H. T. Nembach, M. E. Siemens, S. Eich, C. M. Schneider, T. J. Silva, M. Aeschlimann, M. M.
444 Murnane, and H. C. Kapteyn, Proceedings of the National Academy of Sciences **109**, 4792
445 (2012).
- 446 ¹⁵ E. Carpene, H. Hedayat, F. Boschini, and C. Dallera, Physical Review B **91**, 174414 (2015).
- 447 ¹⁶ D. Hinzke, U. Atxitia, K. Carva, P. Nieves, O. Chubykalo-Fesenko, P. M. Oppeneer, and
448 U. Nowak, Physical Review B **92**, 054412 (2015).
- 449 ¹⁷ A. B. Schmidt, M. Pickel, M. Donath, P. Buczek, A. Ernst, V. P. Zhukov, P. M. Echenique,
450 L. M. Sandratskii, E. V. Chulkov, and M. Weinelt, Physical Review Letters **105**, 197401 (2010).
- 451 ¹⁸ A. R. Khorsand, M. Savoini, A. Kirilyuk, A. V. Kimel, A. Tsukamoto, A. Itoh, and T. Rasing,
452 Phys. Rev. Lett. **110**, 107205 (2013).
- 453 ¹⁹ S. Mathias, C. La-o vorakiat, J. M. Shaw, E. Turgut, P. Grychtol, R. Adam, D. Rudolf, H. T.
454 Nembach, T. J. Silva, M. Aeschlimann, C. M. Schneider, H. C. Kapteyn, and M. M. Murnane,
455 Journal of Electron Spectroscopy and Related Phenomena **189**, 164 (2013).

- ²⁰ E. Turgut, D. Zusin, D. Legut, K. Carva, R. Knut, J. M. Shaw, C. Chen, Z. Tao, H. T. Nembach,
T. J. Silva, S. Mathias, M. Aeschlimann, P. M. Oppeneer, H. C. Kapteyn, M. M. Murnane,
and P. Grychtol, *Physical Review B* **94**, 220408 (2016).
- ²¹ M. F. Tesch, M. C. Gilbert, H.-C. Mertins, D. E. Bürgler, U. Berges, and C. M. Schneider,
Applied Optics **52**, 4294 (2013).
- ²² Z. Q. Qiu and S. D. Bader, *Journal of Magnetism and Magnetic Materials* **200**, 664 (1999).
- ²³ H.-C. Mertins, S. Valencia, A. Gaupp, W. Gudat, P. M. Oppeneer, and C. M. Schneider,
Applied Physics A **80**, 1011 (2005).
- ²⁴ S. Valencia, A. Gaupp, W. Gudat, H.-C. Mertins, P. M. Oppeneer, D. Abramssohn, and C. M.
Schneider, *New Journal of Physics* **8**, 254 (2006).
- ²⁵ S. Valencia, A. Kleibert, A. Gaupp, J. Ruzs, D. Legut, J. Bansmann, W. Gudat, and P. M.
Oppeneer, *Physical Review Letters* **104**, 187401 (2010).
- ²⁶ J. B. Kortright and S.-K. Kim, *Physical Review B* **62**, 12216 (2000).
- ²⁷ H. Höchst, D. Zhao, and D. L. Huber, *Surface Science Proceedings of the 15th European
Conference on Surface Science*, **352**, 998 (1996).
- ²⁸ J. Stöhr and H. C. Siegmann, *Magnetism: From Fundamentals to Nanoscale Dynamics* (Springer
Science & Business Media, 2007).
- ²⁹ C. T. Chen, Y. U. Idzerda, H.-J. Lin, N. V. Smith, G. Meigs, E. Chaban, G. H. Ho, E. Pellegrin,
and F. Sette, *Physical Review Letters* **75**, 152 (1995).
- ³⁰ A. Weber, F. Pressacco, S. Günther, E. Mancini, P. M. Oppeneer, and C. H. Back, *Physical
Review B* **84**, 132412 (2011).
- ³¹ M. Plötzing, R. Adam, C. Weier, L. Plucinski, S. Eich, S. Emmerich, M. Rollinger, M. Aeschli-
mann, S. Mathias, and C. M. Schneider, *Review of Scientific Instruments* **87**, 043903 (2016).
- ³² S. Eich, M. Plötzing, M. Rollinger, S. Emmerich, R. Adam, C. Chen, H. C. Kapteyn, M. M.
Murnane, L. Plucinski, D. Steil, B. Stadtmüller, M. Cinchetti, M. Aeschlimann, C. M. Schneider,
and S. Mathias, *Science Advances* **3**, e1602094 (2017).
- ³³ M. Hecker, S. Valencia, P. M. Oppeneer, H.-C. Mertins, and C. M. Schneider, *Physical Review
B* **72**, 054437 (2005).
- ³⁴ P. M. Oppeneer, H.-C. Mertins, and O. Zaharko, *Journal of Physics: Condensed Matter* **15**,
7803 (2003).
- ³⁵ P. M. Oppeneer, in *Handbook of Magnetic Materials*, Vol. 13, edited by K. H. J. Buschow

487 (Elsevier, Amsterdam, 2001) pp. 229–422.

488 ³⁶ M. Pascolini, S. Bonora, A. Giglia, N. Mahne, S. Nannarone, and L. Poletto, *Applied Optics*
489 **45**, 3253 (2006).

490 ³⁷ P. B. Corkum, *Physical Review Letters* **71**, 1994 (1993).

491 ³⁸ M. Lewenstein, P. Balcou, M. Y. Ivanov, A. L’Huillier, and P. B. Corkum, *Physical Review A*
492 **49**, 2117 (1994).

493 ³⁹ B. L. Henke, E. M. Gullikson, and J. C. Davis, *Atomic Data and Nuclear Data Tables* **54**, 181
494 (1993).

495 ⁴⁰ L. Guidoni, E. Beaurepaire, and J.-Y. Bigot, *Physical Review Letters* **89**, 017401 (2002).

496 ⁴¹ K. Carva, M. Battiato, and P. M. Oppeneer, *Physical Review Letters* **107**, 207201 (2011).

497 ⁴² M. Föhnle, T. Tsatsoulis, C. Illg, M. Haag, B. Y. Müller, and L. Zhang, *Journal of Supercon-*
498 *ductivity and Novel Magnetism* **30**, 1381 (2017).

499 ⁴³ C. Illg, M. Haag, and M. Föhnle, *Physical Review B* **88**, 214404 (2013).

500 ⁴⁴ M. Haag, C. Illg, and M. Föhnle, *Physical Review B* **90**, 014417 (2014).

501 ⁴⁵ U. Atxitia, O. Chubykalo-Fesenko, N. Kazantseva, D. Hinzke, U. Nowak, and R. W. Chantrell,
502 *Applied Physics Letters* **91**, 232507 (2007).

503 ⁴⁶ W. Hübner and G. P. Zhang, *Physical Review B* **58**, R5920 (1998).

504 ⁴⁷ A. J. Schellekens and B. Koopmans, *Physical Review Letters* **110**, 217204 (2013).

505 ⁴⁸ E. C. Stoner, *Proceedings of the Royal Society of London A: Mathematical, Physical and En-*
506 *gineering Sciences* **165**, 372 (1938).

507 ⁴⁹ C. Herring and C. Kittel, *Physical Review* **81**, 869 (1951).

508 ⁵⁰ M. P. Gokhale and D. L. Mills, *Physical Review B* **49**, 3880 (1994).

509 ⁵¹ J. L. Erskine and E. A. Stern, *Physical Review B* **12**, 5016 (1975).

510 ⁵² P. M. Oppeneer, J. Sticht, T. Maurer, and J. Kübler, *Zeitschrift für Physik B Condensed*
511 *Matter* **88**, 309 (1992).

512 ⁵³ M. Stamenova, J. Simoni, and S. Sanvito, *Physical Review B* **94**, 014423 (2016).

513 ⁵⁴ J.-Y. Bigot, M. Vomir, and E. Beaurepaire, *Nature Physics* **5**, 515 (2009).

514 ⁵⁵ Z. J. Yang and M. R. Scheinfein, *Journal of Applied Physics* **74**, 6810 (1993).

515 ⁵⁶ C. La-O-Vorakiat, M. Siemens, M. M. Murnane, H. C. Kapteyn, S. Mathias, M. Aeschlimann,
516 P. Grychtol, R. Adam, C. M. Schneider, J. M. Shaw, H. Nembach, and T. J. Silva, *Physical*
517 *Review Letters* **103**, 257402 (2009).

- ⁵¹⁸ ⁵⁷ J. Zak, E. R. Moog, C. Liu, and S. D. Bader, Physical Review B **43**, 6423 (1991).
- ⁵¹⁹ ⁵⁸ M. G. Moharam and T. K. Gaylord, JOSA **71**, 811 (1981).
- ⁵²⁰ ⁵⁹ M. G. Moharam, T. K. Gaylord, E. B. Grann, and D. A. Pommert, JOSA A **12**, 1068 (1995).
- ⁵²¹ ⁶⁰ M. G. Moharam, T. K. Gaylord, D. A. Pommert, and E. B. Grann, JOSA A **12**, 1077 (1995).